Am J Transl Res 2025;17(4):2562-2576
www.ajtr.org /ISSN:1943-8141/AJTR0163012

Original Article

Single-cell RNA sequencing of adult primate neocortex reveals the regulatory dynamics of neural plasticity

Chi Zhang[1], Zihong Xie[2], Ningli Wang[1]

[1]*Beijing Tongren Eye Center, Beijing Tongren Hospital, Capital Medical University, Beijing 100730, China;* [2]*State Key Laboratory of Ophthalmology, Zhongshan Ophthalmic Center, Sun Yat-sen University, Guangzhou 510060, Guangdong, China*

Received December 31, 2024; Accepted March 11, 2025; Epub April 15, 2025; Published April 30, 2025

Abstract: Objectives: To investigate gene expression dynamics in adult primate neocortex and elucidate the molecular basis of these capabilities. Methods: Whole-cell transcriptome data from primary visual cortex (V1) of cynomolgus monkeys were analyzed, focusing on inhibitory neurons derived from the medial ganglionic eminence. Using RNA velocity and scVelo algorithms, we investigated subtle gene expression shifts, identified key driver genes, and conducted functional enrichment analysis. Results: Our analysis revealed that somatostatin (*SST*)+ neurons are generated prior to parvalbumin (*PVALB*)+ neurons, with gene expression trajectories resembling those observed in developing animals. However, certain well-established *SST*+ and *PVALB*+ neurons, such as long-projecting *SST*+ chondrolectin (*CHODL*)+ neurons and *PVALB*+ unc-5 netrin receptor B (*UNC5B*)+ neurons, do not share the same lineage, suggesting distinct regulatory programs. Furthermore, we identified a set of genes strongly correlated with these trajectories, including dihydropyrimidinase like 3 (*DPYSL3*), osteocrin (*OSTN*), smoothelin (*SMTN*), meis homeobox 2 (*MEIS2*), chromodomain helicase DNA binding protein 3 (*CHD3*), and chromodomain helicase DNA binding protein 5 (*CHD5*). Functional enrichment analysis suggested that these genes are associated with neural plasticity and axon growth. Conclusions: This study provides novel insights into the gene expression dynamics of the primate neocortex. Genes involved in neuronal development and plasticity may underlie the advanced information-processing capabilities in primates.

Keywords: Neuronal plasticity, primary visual cortex, Sc-RNA-seq

Introduction

Mammals develop complex neural networks with high plasticity to adapt to their ever-changing environments, which are closely related to both the basic and higher brain functions. However, neurogenesis is limited to a few specific regions in adult mammals, and most existing neurons undergo a prolonged maturation and refinement process shaped by local signaling [1]. The extent to which adult neural networks can be modified, as well as the core regulatory programs that enable mature neuron subtypes to maintain both their identity and plasticity, remain unclear.

The primary visual cortex (V1) of adult macaques offers an ideal model to explore these questions [2]. As diurnal animals, primates depend heavily on visual information and have evolved trichromatic and stereoscopic vision with high precision. Anatomical and electrophysiological studies have identified primate-specific structures, such as ocular dominance columns and an expanded layer (L4) [3-5]. Visual experience drives network plasticity during the critical period of postnatal visual development, primarily through interaction between local signaling and intrinsic gene-expression regulation [6]. Even in adulthood, the visual system maintains high levels of plasticity in primates [2, 7]. Investigating the subtle divergencies and similarities among neurons of the same cell type can provide insights into the core transcriptomic programs that govern plasticity and maintain cellular identity and functions.

The rise of digital technologies has created unparalleled opportunities in the global health-

https://doi.org/10.62347/ZEOR5569

care sector [8]. Recent advancements in high-throughput sequencing enable high-resolution classification of neuronal cell types [2, 9-16]. Transcriptomic signatures have been established for various neuronal populations, including glutamatergic and GABAergic neurons. Glutamatergic neurons are excitatory and classified based on their laminar distribution and predicted projection targets. In contrast, GABAergic neurons are inhibitory and can be further subdivided by their origin into two branches: the lim homeobox 6 (*LHX6*)+ branch, derived from the medial ganglionic eminence (MGE), and the nuclear receptor subfamily 2 group f member 2 (*NR2F2*)+ branch, originating from the caudal ganglionic eminence (CGE). The MGE-derived branch includes the parvalbumin (*PVALB*)+ and somatostatin (*SST*)+ subclasses, while the CGE-derived branch consists of the lysosomal-associated membrane protein family member 5 (*LAMP5*)+, vasoactive intestinal peptide (*VIP*)+, and adenosine deaminase RNA-specific b2 (*ADARB2*)+/paired box 6 (*PAX6*)+ (synuclein gamma (*SNCG*)+) subclasses [2]. GABAergic neurons synapse on local neurons and fine-tune the network in an experience-dependent manner. However, detailed analyses of GABAergic neurons, especially those within the same lineage (such as the MGE-derived *PVALB*+ and *SST*+ neurons), and the genes that drive and maintain transcriptomic diversity, have not been fully explored.

In this study, we utilized a whole-cell single-cell RNA sequencing dataset from the primary visual cortex of macaque monkeys to analyze transcriptomic shifts within one of the most well-characterized inhibitory lineages, the MGE lineage. Using the RNA velocity algorithm, which captures transcriptomic shifts at single-cell resolution by assessing both spliced and unspliced RNA abundance, we identified a conserved group of mature adult neurons [17, 18]. Enrichment analysis revealed that genes associated with these transcriptomic shifts are linked to neuroplasticity, providing molecular insights into how mature neurons maintain core functions while preserving appropriate levels of plasticity.

Materials and methods

Data acquisition

The Macaque V1 10× Genomics dataset was downloaded from the European Molecular Biology Laboratory's (EMBL) European Bioinformatics Institute (EBI) database (https://www.ebi.ac.uk/) under the accession code E-MTAB-10459 [2].

Data preprocessing

Cell Ranger (version 3.0.2, 10× Genomics) was used to process the raw output from Chromium Single Cell 3' RNA-seq. Cells with fewer than 200 features or those exhibiting more than 30% mitochondrial content were removed for quality control. Additionally, features expressed in fewer than 10 cells were also excluded. Data processing, analysis, and visualization were performed using SCANPY (version 1.4.6) [19]. Scrublet (version 0.2.1) was used to identify and exclude potential cell doublets [20], which were detected based on cluster analysis, where a Scrublet score was computed for each cluster, indicating the likelihood of doublet presence. Clusters with high Scrublet scores in t-SNE or UMAP (detailed below) and with marker gene expression patterns overlapping multiple clusters were classified as cell doublets and excluded from further analysis.

Data processing, analysis, and visualization

Data processing, analysis, and visualization were performed sequentially using SCANPY. Data normalization: Gene expression counts were normalized to counts per 10,000 (NC) by dividing the total mapped exonic reads for each gene by the total number of mapped reads in the cell, then multiplying by 10,000. This method generates a value equivalent to one-hundredth of counts per million (CPM). Log transformation: A log2 (NC + 1) transformation was applied to stabilize variance and approximate a normal distribution. Highly Variable Genes (HVG) Selection: HVGs were selected from the log-transformed data for further analysis. Principal Component Analysis (PCA): PCA was conducted on the selected HVGs to reduce dimensionality of the dataset while preserving the majority of variance. If necessary, HVGs and PCA were recalculated for specific cell subsets.

Data integration and correction were conducted using Harmony (version 0.0.5) based on PCA embeddings [21]. The corrected data minimized both technical factors and biological variations.

Dimension reduction and clustering were performed using SCANPY. Neighborhood calculation: The local neighborhoods were calculated using the scanpy.pp.neighbors function, constructing a k-nearest neighbors (knn) graph based on Harmony-corrected PCA embeddings. The number of local neighborhoods was set to 15, using all 50 Harmony-corrected PCs. Uniform Manifold Approximation and Projection (UMAP)/T-distributed stochastic neighbor embedding (t-SNE) [22-25]: Both UMAP and t-SNE were performed using Euclidean distance. UMAP was computed using the scanpy.tl.umap function with the following parameters: minimal effective distance = 0.5, spread = 1.0, initial learning rate = 1.0, negative sample weighting = 1.0, and negative edge sample rate = 5. t-SNE was computed using scanpy.tl.tsne. Louvain clustering [26]: Louvain clustering was applied using the sc.tl.louvain function on the neighborhood graph generated in the previous steps. The analysis was conducted with the resolution parameter set to 2, using the vtraag package, without applying weights from knn graph. The resolution parameter was adjusted between 1 and 5 to achieve finer cluster divisions. Single-Cell Clustering Assessment Framework (SCCAF) [27]: SCCAF (version 0.0.10) was used with the SCCAF_assessment function to evaluate the quality and robustness of the clusters. For five-fold cross-validation training, 200 cells from each cluster were selected. The remaining cells were utilized to evaluate segregation accuracy. Clusters with a segregation accuracy greater than 84% on the hold-out set were considered acceptable.

Differential expression analysis

Differentially expressed genes (DEGs) between clusters were identified using the Model-based Analysis of Single-cell Transcriptomics (MAST), which applies a hurdle model to account for both technical effects and biological variabilities [28]. The top 200 DEGs from each cell cluster were selected for Gene Ontology (GO) and Kyoto Encyclopedia of Genes and Genomes (KEGG) enrichment analyses [29-33]. Gene Set Enrichment Analysis (GSEA) and gProfiler were used to perform GO and KEGG enrichment analyses [34-36].

RNA velocity analysis

RNA velocity analysis was conducted using RNA velocyto (version 0.17.15) and scVelo (version 0.2.2) [17, 18]. RNA velocyto was run on the 10× Cell Ranger using the run 10× option. The UCSC genome GTF file provided organism-specific annotations, while the macaque genome GTF file served as the reference for genome annotation [37]. After generating loom files, scVelo was applied by merging these files with the AnnData object in SCANPY.

The standard scVelo pipeline was used to calculate RNA velocity. Data preprocessing involved filtering for genes with a minimum of 20 counts (both unspliced and spliced) to retain those with sufficient expression for further analysis. Moments were computed for each cell based on its nearest neighbors. The neighbor graph was constructed using Euclidean distances in the PCA embeddings, utilizing 30 principal components and connecting 30 neighbors in connectivity mode. The UMAP method was then applied using the previously selected highly variable genes. Full splicing kinetics for genes were recovered using the scvelo.tl.recover_dynamics function with default settings. The velocities were estimated using the scvelo.tl.velocity function in dynamical mode. The velocity graph, embedded on the UMAP for visualization, was generated using the scvelo.tl.velocity_graph function with default settings.

Tissue procurement

Macaque V1 tissue samples were generously provided by Professor Hao from the Zhongshan Ophthalmic Center. The V1 regions were fixed in 4% paraformaldehyde (PFA) for subsequent Nissl staining and immunofluorescence analysis.

Nissl staining

Nissl staining was performed using the NeuroTrace™ 530/615 red fluorescent Nissl stain kit (Injeka, N21482). Tissue slices were fixed in 4% PFA at 4°C for 1 h, followed by dehydration through increasing sucrose concentrations (10%, 15%, and 30%) and three washes with phosphate-buffered saline (PBS). Permeabilization was achieved using 0.1% Triton X-100 for 10 min, followed by a 5-minute

PBS wash. The slices were then incubated with the NeuroTrace stain for 20 min, washed in PBS for 10 min, and mounted with DAPI (Abcam, AB 104139). Images were captured using a laser scanning confocal fluorescence microscope (Zeiss LSM 880).

Immunofluorescence

Tissues were fixed in 4% PFA at 4°C overnight, and then dehydrated in a 30% sucrose solution at 4°C. They were then embedded in an optimal cutting temperature (OCT; Tissue-Tek) compound and frozen at -80°C. The tissues were sectioned into 30 μm slices using a cryostat microtome (Leica CM 1950). The slices were washed in PBS and blocked for 1 h at room temperature with a solution containing 5% BSA, 1% normal goat serum (Jackson ImmunoResearch, 005000121), and 0.3% Triton X-100 in PBS. Primary antibody incubation was performed overnight at 4°C. After three PBS washes, the slices were incubated with secondary antibodies for 1 h at room temperature. The primary antibodies used included anti-Parvalbumin (1:500, P3088, Sigma, USA), anti-Somatostatin (1:100, ab37008, Abcam, USA), anti-Dihydropyrimidinase Like 3 (1:1000, HPA010948, Sigma, USA), anti-Meis Homeobox 2 (1:100, H00004212-M01, Abnova, USA), and anti-Calcyon (1:500, AB15040, Millipore, USA). The secondary antibodies included Alexa Fluor 647 anti-rat (Invitrogen, A78947, 1:1000), Alexa Fluor 488 anti-rabbit (Invitrogen, A-21206, 1:1000), and Alexa Fluor 555 anti-mouse (Invitrogen, A-31570, 1:1000). After three PBS washes, the slices were mounted with medium containing DAPI (Abcam, ab104139). Images were captured using a laser scanning confocal fluorescence microscope (Zeiss LSM 880).

Results

Molecular taxonomy of MGE-derived inhibitory neurons

To elucidate the transcriptomic dynamics of mature MGE-derived GABAergic neurons, we reanalyzed a well-established dataset of whole-cell transcriptomes from the V1 of cynomolgus monkeys (*Macaca fascicularis*). The dataset included both spliced RNAs in the cytosol and unspliced RNAs in the nucleus, preserving comprehensive transcriptional information (**Figure 1A**). The dataset contained 133,454 cells, which were classified into 26 clusters (**Figure 1B-D**). These clusters were subsequently grouped into the major cell types present in the neocortex: astrocytes, excitatory neurons (Exc), inhibitory neurons (Inh), microglia, oligodendrocyte progenitor cells (OPC), oligodendrocytes (Oligo), and vascular cells (**Figure 1C**). Further subdivision of the excitatory and inhibitory neurons revealed four and five subclasses, respectively, based on the expression of specific cell markers (**Figure 1E**, **1F**).

Among the total 133,454 cells, 12,097 inhibitory neurons (9%) were identified based on canonical marker expression. The MGE-derived cells were selected based on the expression of *PVALB*, *SST*, and corresponding cell labels, yielding 1,572 *PVALB*+ and *SST*+ neurons (**Figure 2A**). The expression of well-established MGE lineage marker genes, including synaptosome-associated protein 25 (*SNAP25*), *LHX6*, and glutamate decarboxylase 1 (*GAD1*), as well as the layer distribution of the dataset, is illustrated in **Figure 2B**. Based on these canonical markers, the *PVALB*+ and *SST*+ neurons were further subdivided into 6 and 8 transcriptomic cell types, respectively (**Figure 2C**). The proportions of each cell type were calculated and illustrated in **Figure 2D**.

RNA velocity reveals transcriptomic shifts in MGE-derived inhibitory neurons

To determine where cellular dynamics regulated by driver genes during neuronal development persist in mature primate neurons, we conducted RNA velocity analysis using scVelo. This allowed us to systematically identify the key factors and pathways involved in the development of MGE-derived *PVALB*+ and *SST*+ neurons [17, 18]. All transcriptomic cell types of the *PVALB*+ and *SST*+ neurons were included in future analyses. ScVelo predicted that *SST*+ neurons give rise to the *PVALB*+ neurons (**Figure 3A**). Here, we found that *SST*+ complexin 2 (*CPLX2*)+ neurons, originating from *SST*+ *GPM6A*+ neurons, differentiate into *PVALB*+ immunoglobulin superfamily containing leucine-rich repeat 2 (*ISLR2*)+ neurons, followed by *PVALB*+ regulator of G protein signaling 5 (*RGS5*)+ neurons, and ultimately *PVALB*+ osteocrin (*OSTN*)+ neurons. In addition, *SST*+ triadin (*TRDN*)+ neurons branch

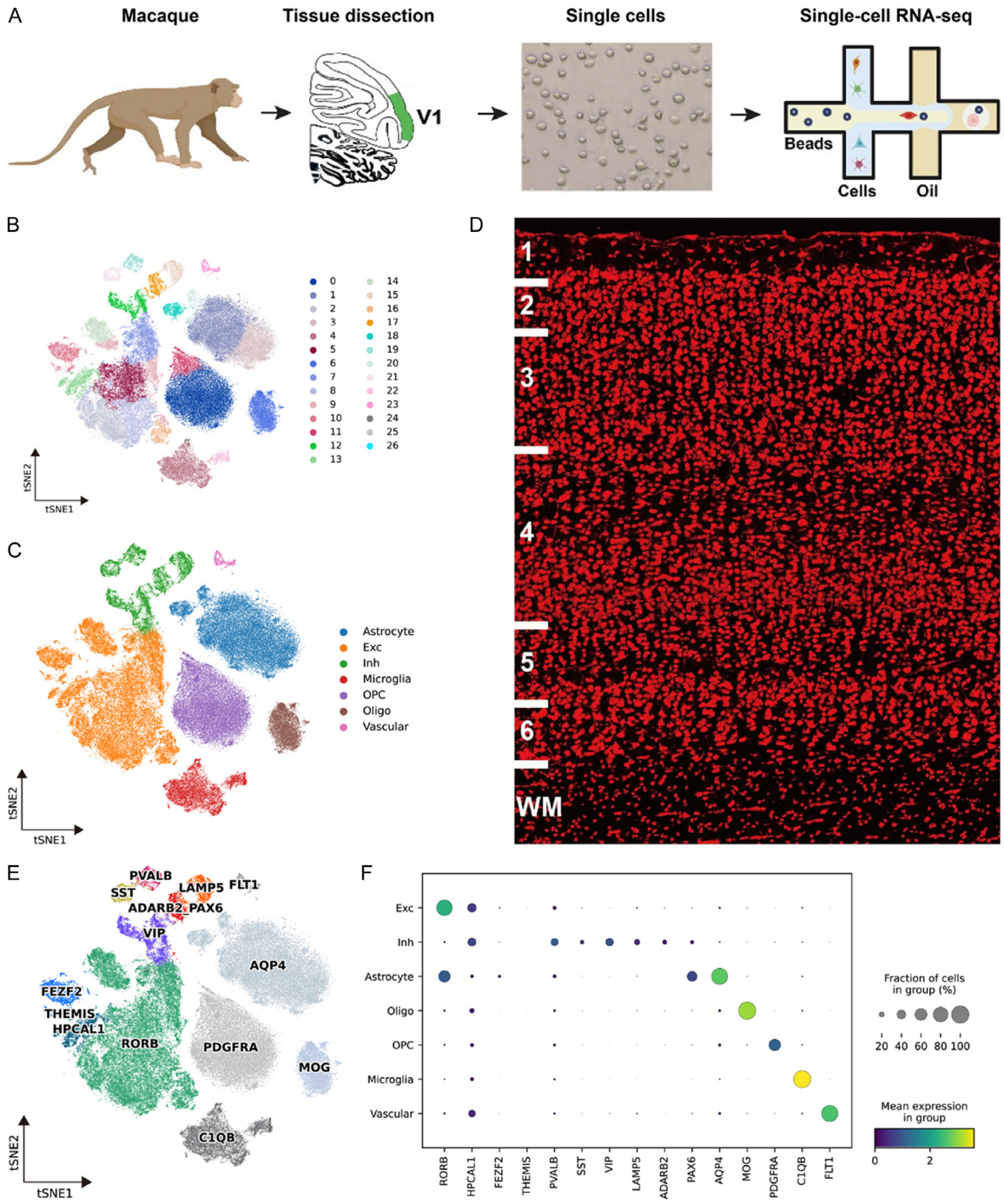

Figure 1. Flow diagram and cell type classification in macaque primary visual cortex (V1). A. Illustration diagram of single-cell transcriptome analysis in macaque V1. The V1 region selected for single-cell isolation is highlighted in green. Illustrations of the macaque and individual cells were created using the BioRender platform (www. BioRender.com). B. tSNE visualization of the 26 original clusters of total cells from the cynomolgus monkey V1. C. tSNE visualization of the total cells, colored by cell type. D. Nissl staining of the macaque V1, showing cortical layers 1-6 (L1-6) of the neocortex. WM, white matter. E. tSNE visualization of the total cells, colored by marker gene expression. Excitatory neuron markers: Hippocalcin-like 1 (*HPCAL1*), rar-related orphan receptor b (*RORB*), FEZ family zinc finger 2 (*FEZF2*), thymocyte selection-associated (*THEMIS*); Inhibitory neuron markers: parvalbumin (*PVALB*), somatostatin (*SST*), vasoactive intestinal peptide (*VIP*), lysosomal-associated membrane protein family member 5 (*LAMP5*), adenosine deaminase RNA-specific B2 (*ADARB2*)_paired box 6 (*PAX6*); Astrocyte marker: aquaporin 4 (*AQP4*); Oligodendrocyte marker: myelin oligodendrocyte glycoprotein (*MOG*); Microglia markers: platelet-derived growth factor receptor alpha (*PDGFRA*), oligodendrocyte progenitor cell marker; complement c1q B chain (*C1QB*); Vascular cell marker: FMS-related receptor tyrosine kinase 1 (*FLT1*). Red circles indicate medial ganglionic eminence (MGE) lineages of *PVALB*+ and *SST*+ neurons. F. Dotplot shows marker gene expression in the total cells.

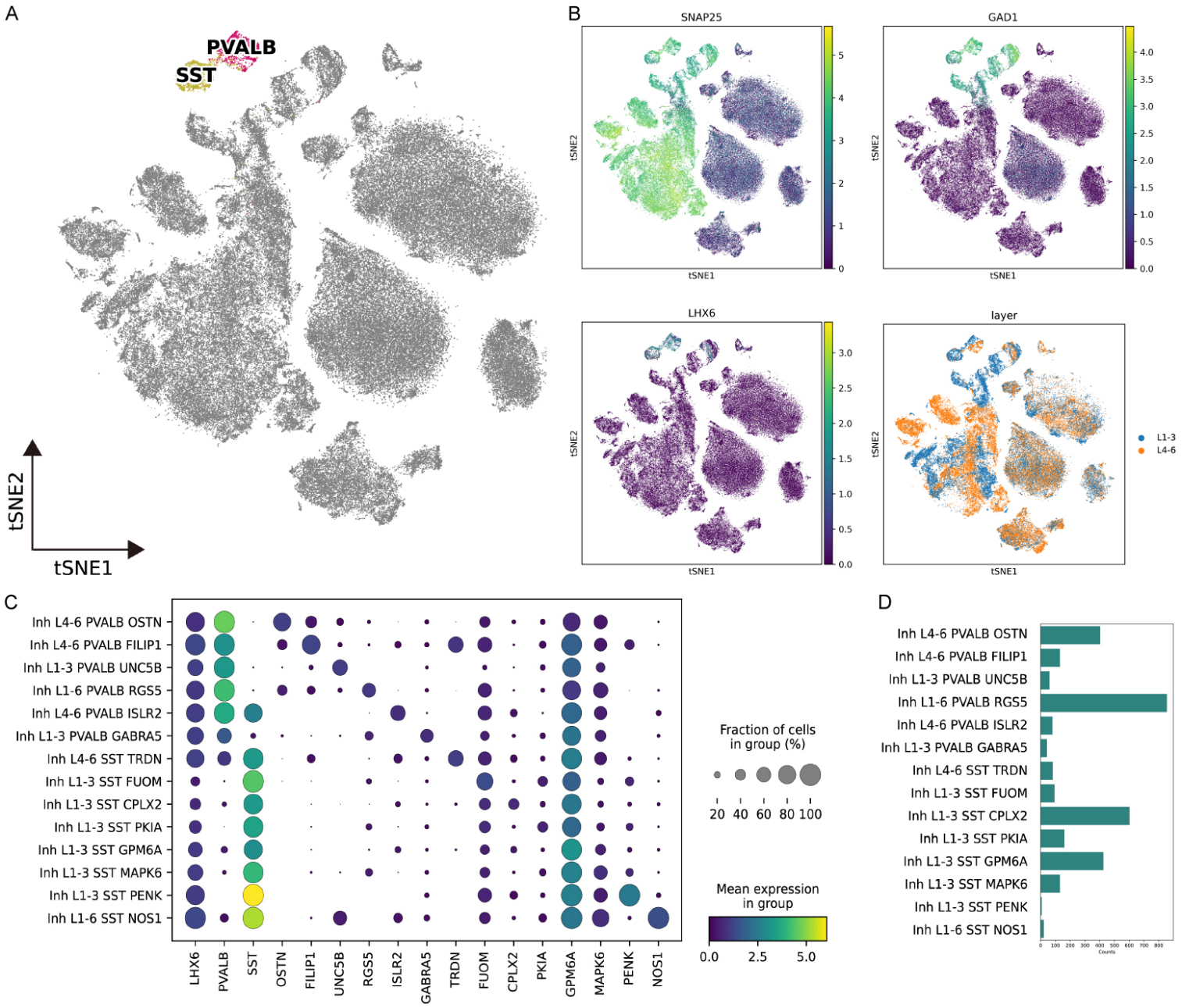
A
PVALB
SST
tSNE2
tSNE1
B
SNAP25
GAD1
LHX6
layer
tSNE1
tSNE2
L1-3
L4-6
C
Inh L4-6 PVALB OSTN
Inh L4-6 PVALB FILIP1
Inh L1-3 PVALB UNC5B
Inh L1-6 PVALB RGS5
Inh L4-6 PVALB ISLR2
Inh L1-3 PVALB GABRA5
Inh L4-6 SST TRDN
Inh L1-3 SST FUOM
Inh L1-3 SST CPLX2
Inh L1-3 SST PKIA
Inh L1-3 SST GPM6A
Inh L1-3 SST MAPK6
Inh L1-3 SST PENK
Inh L1-6 SST NOS1
LHX6 PVALB SST OSTN FILIP1 UNC5B RGS5 ISLR2 GABRA5 TRDN FUOM CPLX2 PKIA GPM6A MAPK6 PENK NOS1
Fraction of cells in group (%)
20 40 60 80 100
Mean expression in group
0.0 2.5 5.0
D
Counts

Figure 2. MGE-derived cell taxonomy in the macaque V1. A. tSNE visualization of MGE-derived cells (indicated by circles) using the same color scheme shown in **Figure 1C**, with all other cells shown in gray. B. tSNE visualization of the expression of the canonical marker genes for MGE-derived cells and the layer distribution within the datasets. C. Dotplot showing the marker gene expression in MGE-derived cells. D. Proportional representations of different MGE-derived cell types.

from *SST*+*GPM6A*+ neurons. Notably, *SST*+ fucose mutarotase (*FUOM*)+ neurons differentiate into *SST*+ CAMP-dependent protein kinase inhibitor alpha (*PKIA*)+ neurons, then *SST*+ mitogen-activated protein kinase 6 (*MAPK6*)+ neurons, and eventually give rise to *PVALB*+ gamma-aminobutyric acid type A receptor subunit alpha 5 (*GABRA5*)+ neurons. ScVelo also predicted that *SST*+ proenkephalin (*PENK*)+ neurons and *SST*+ chondrolectin (*CHODL*)+ neurons are independent of other neuron populations, with no predicted trajectories leading to other neuron types. Similarly, *PVALB*+ unc-5 netrin receptor B (*UNC5B*)+ neurons and *PVALB*+ filamin A interacting protein 1 (*FILIP1*)+ neurons exhibited distinct origins, suggesting separate developmental pathways.

The selective driver genes correlated with these developmental trajectories are illustrated in **Figure 3B**, **3D**, with representative gene expressions validated in **Figure 3C**, **3E**. Dihydropyrimidinase-like 3 (*DPYSL3*), *OSTN*, and smoothlin (*SMTN*) appear to drive neurons towards the *PVALB*+ cell fate, while meis homeobox 2 (*MEIS2*), chromodomain helicase DNA binding protein 3 (*CHD3*), and chromodomain helicase DNA binding protein 3 (*CHD5*) seem to drive neurons towards the *SST*+ cell fate.

Next, we calculated the latent time of the cells in the MGE lineages (**Figure 4A**). The latent time for *SST*+ neurons was lower compared to the *PVALB*+ neurons, which exhibited higher latent times. Putative driver genes correlated with these latent time differences were identified and visualized in a heatmap (**Figure 4B**). A shared driver gene, *PVALB*+ *SST*+ calcyon neuron specific vesicular protein (*CALY*), was validated in **Figure 4C**, and gene expression patterns across each cell type are illustrated in **Figure 4D**.

GO biological process enrichment analysis revealed that, in addition to the nervous system development process, the identified genes are involved in cell morphology and projection, cell adhesion, cell-cell communication, and most interestingly, axon genesis [34, 35]. These processes are predominantly focused on anatomical structure morphogenesis, cell communication, and signaling. Furthermore, KEGG pathway enrichment analysis revealed that these genes are mainly associated with neurodegeneration pathways, calcium signaling, and axon guidance. These results suggest that major modifications in mature neurons are likely related to axon growth, particularly involving projections to new areas through the formation of new synapses (**Figure 5A**, **5B**).

Discussion

In this study, we analyzed the transcriptomic shifts within the MGE-derived inhibitory neurons in the macaque primary visual cortex. Our findings revealed that *SST*+ neurons are generated prior to *PVALB*+ neurons, mirroring developmental patterns observed in earlier stages of tissue development. However, long-projecting *SST*+*CHODL*+ neurons and *PVALB*+ *UNC5B*+ neurons did not share the same lineage, suggesting distinct regulatory mechanisms. We identified a set of genes correlated with the neural development trajectories, which are linked to neural plasticity and axon growth. These genes offer insights into the enhanced information-processing capabilities of the primate neocortex.

Previous studies have established a detailed genetic cascade within the mouse MGE lineage [17]. Consistent with earlier research on mice, our study found that *SST* neurons give rise to *PVALB* neurons [38-40]. Although scVelo analysis is traditionally used in developing tissues, accumulating evidence suggests that gene expression in mature neurons remains under the regulation of transcription factors [41]. Our findings align with these developmental patterns, even in mature neuronal populations.

We identified selective driver genes that correlate with the developmental trajectories of MGE-derived neurons, including *DPYSL3*, *OSTN*, *SMTN*, *MEIS2*, *CHD3*, and *CHD5*. These genes are associated with neuronal develop-

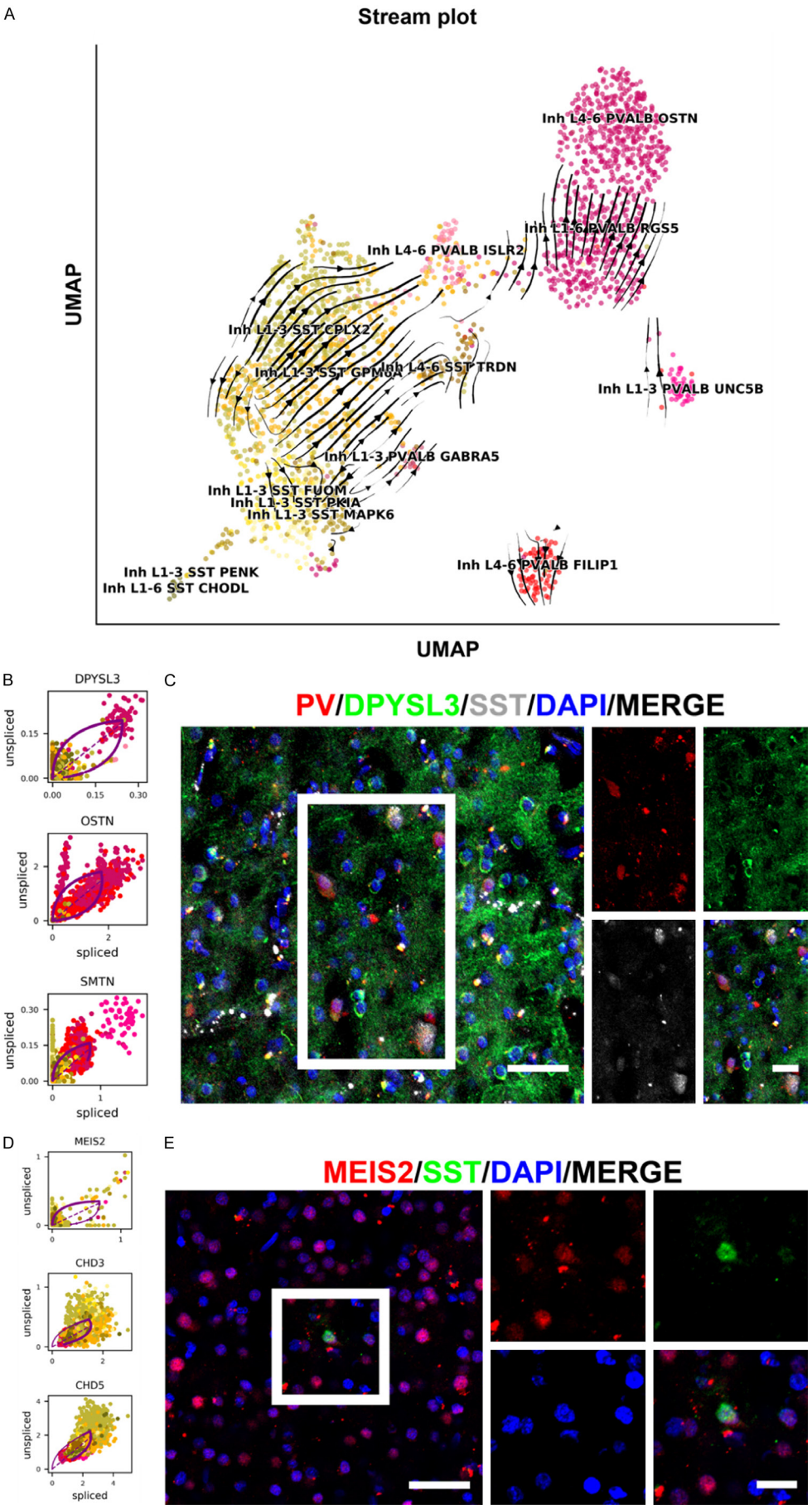
A
Stream plot
UMAP
UMAP
Inh L4-6 PVALB OSTN
Inh L4-6 PVALB RGS5
Inh L4-6 PVALB ISLR2
Inh L1-3 SST CPLX2
Inh L1-3 SST GPM6A
Inh L4-6 SST TRDN
Inh L1-3 PVALB UNC5B
Inh L1-3 PVALB GABRA5
Inh L1-3 SST FUOM
Inh L1-3 SST PKIA
Inh L1-3 SST MAPK6
Inh L1-3 SST PENK
Inh L1-6 SST CHODL
Inh L4-6 PVALB FILIP1
B
DPYSL3
OSTN
SMTN
unspliced
spliced
C
PV/DPYSL3/SST/DAPI/MERGE
D
MEIS2
CHD3
CHD5
unspliced
spliced
E
MEIS2/SST/DAPI/MERGE

Figure 3. Dynamics of the *SST* to *PVALB* transition recapitulated by scVelo. (A) scVelo analysis of developmental trajectories for *PVALB*+ and *SST*+ subclasses with regulatory dynamics indicated by black arrows. (B) Example of tentative PV-related driver genes identified with high likelihoods by scVelo. The cells follow the same color scheme as shown in (A). (C) Immunostaining of *PVALB*, dihydropyrimidinase-like 3 (*DPYSL3*) and *SST*. DAPI, nuclei. Scale bar, 40 μm (low magnification) and 20 μm (high magnification). (D) Example of tentative PVALB-related driver genes identified with high likelihoods by scVelo. The cells follow the same color scheme shown in (A). (E) Immunofluorescent staining of meis homeobox 2 (*MEIS2*) and *SST*. DAPI, nuclei. Scale bar, 40 μm (low magnification) and 20 μm (high magnification).

ment, plasticity, and connectivity. For instance, *DPYSL3* plays a critical role in neuronal development and function, including neurite and axonal outgrowth, neuronal differentiation, axonal guidance and regeneration, and proapoptotic signal transduction [42]. *OSTN,* which is induced by sensory stimuli, regulates activity-dependent dendritic growth in neurons [43]. *SMTN* is a cytoskeletal protein contributing to cellular structural stability. *MEIS2* is essential for regulating neural tube patterning, neural progenitor cell proliferation, cell-fate acquisition, neuronal maturation, neurite outgrowth, and synaptogenesis [44]. *CHD5* is involved in early radial migration, while *CHD3* is crucial for late migration and laminar specification of neurons [45]. These driver genes likely contribute to neuronal morphological plasticity, functional differentiation, and network integration, thereby enhancing the information-processing capacity of the primate neocortex.

Consistent with previously established maturation processes, our study found that the latent time for *SST*+ neurons is shorter than that for *PVALB*+ neurons. The putative driver genes correlated with latent time include *CALY*, a disintegrin and metalloproteinase with thrombospondin motifs (*ADAMTS*), protocadherin-19 (*PCDH19*), and talin 2 (*TLN2*). *CALY* is involved in endocytic and recycling processes, playing roles in neuronal development, synaptic function, and neurodegeneration [46]. *ADAMTS* encodes a secreted enzyme that regulates synaptic and neurite plasticity by influencing the extracellular matrix of the central nervous system [47]. *PCDH19* encodes a calcium-dependent adhesion molecule that plays a role in signal transduction at synapses, and is associated with cell adhesion, neuronal migration, and synaptic plasticity [48, 49]. *TLN2* is crucial for the formation of actin filaments and the spreading and migration of various cell types [50]. Together, these genes likely form a network that supports the development, connectivity, and plasticity of neural circuits, shedding light on the complex mechanisms behind synaptic plasticity and neuronal function in the primate brain.

Evolution has driven significant modifications in both the structure and function of the brain. In primates, complex sensory processing demands have led to evolutionary enhancements across various cortical regions. In macaque V1, specialized structures such as ocular dominance columns, an expanded L4, and enlarged macular receptive fields have been identified [51-53]. These adaptations suggest that specific cell types and intricate neural circuits play a critical role in supporting sophisticated visual functions. The laminar organization of macaque V1, as demonstrated by Nissl staining and molecular patterns at the cellular level, closely resembles that of human V1 [5]. This similarity makes macaque V1 an ideal model for exploring the cellular and molecular mechanisms underlying brain evolution across species, particularly in the context of higher-order primates like humans. These cell types and circuits are shaped by experience, allowing individuals to adapt their behavior to the surrounding environment in unique ways. Unlike rodents, primates are diurnal animals with flat eyes that receive binocular light stimuli. The differences in visual experience between primates and rodents may be attributed to the emergence of novel cell types or the modification of existing networks, which can be elucidated through large-scale, high-throughput analysis of cortical neurons.

From mice to primates, mammals share a basic neural framework for processing sensory information [54]. However, neonatal primates demonstrate very limited, if any, advantages in visual perception over mice, suggesting that innate circuits alone do not account for the advanced sensory processing seen in adult primates. Instead, these innate circuits are extensively shaped by experience [55]. For example, deprivation amblyopia caused by congeni-

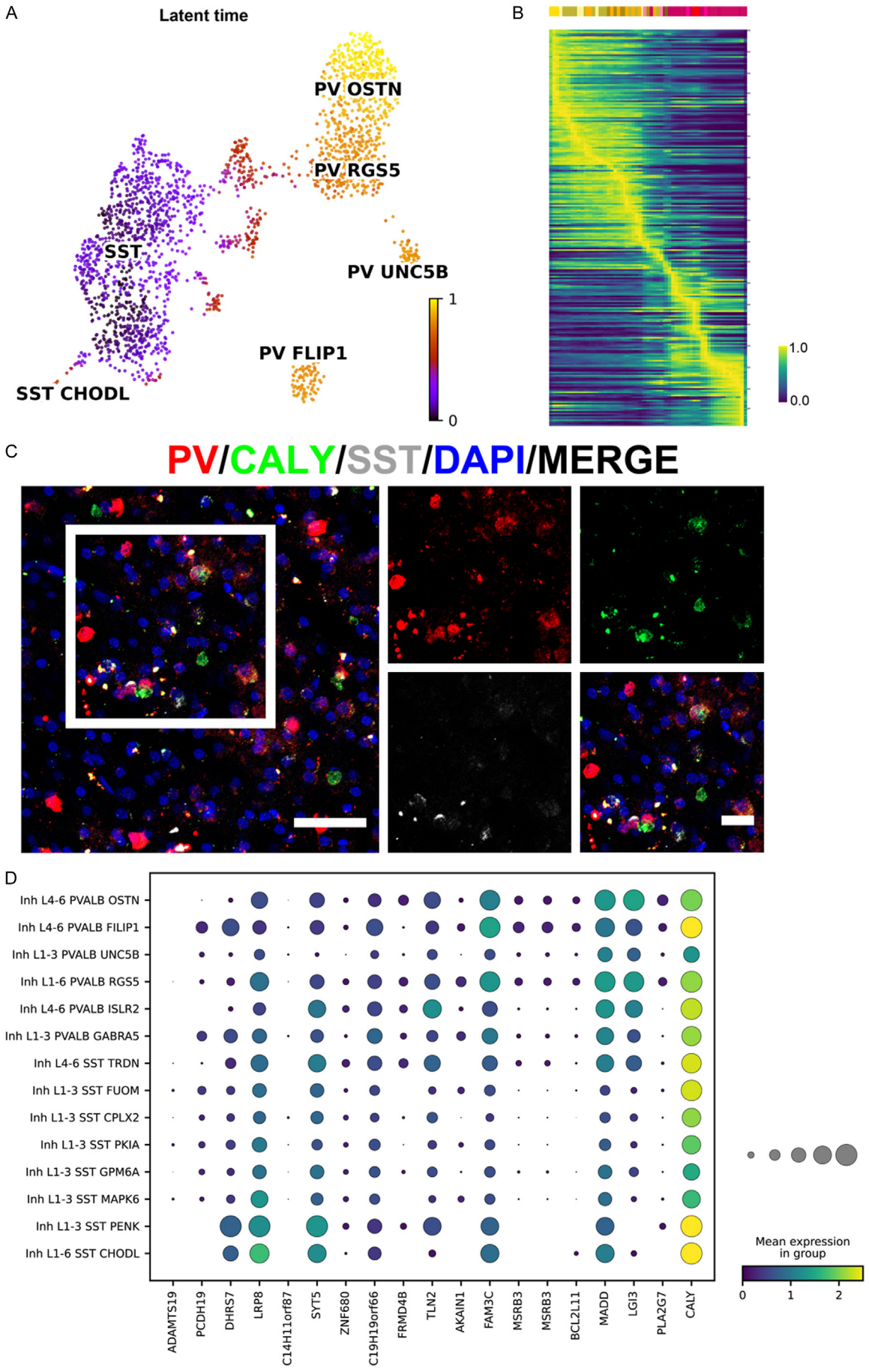
A
Latent time
PV OSTN
PV RGS5
SST
PV UNC5B
PV FLIP1
SST CHODL
1
0
B
1.0
0.0
C
PV/CALY/SST/DAPI/MERGE
D
Inh L4-6 PVALB OSTN
Inh L4-6 PVALB FILIP1
Inh L1-3 PVALB UNC5B
Inh L1-6 PVALB RGS5
Inh L4-6 PVALB ISLR2
Inh L1-3 PVALB GABRA5
Inh L4-6 SST TRDN
Inh L1-3 SST FUOM
Inh L1-3 SST CPLX2
Inh L1-3 SST PKIA
Inh L1-3 SST GPM6A
Inh L1-3 SST MAPK6
Inh L1-3 SST PENK
Inh L1-6 SST CHODL
ADAMTS19
PCDH19
DHRS7
LRP8
C14H11orf87
SYT5
ZNF680
C19H19orf66
FRMD4B
TLN2
AKAIN1
FAM3C
MSRB3
MSRB3
BCL2L11
MADD
LGI3
PLA2G7
CALY
Mean expression in group
0
1
2

Figure 4. Gene expression dynamics revealed by latent time. A. UMAPs colored by the corresponding scVelo-inferred latent time, ranging from early (deep purple) to late (yellow). B. Heatmap of tentative driver genes involved in the maturation process of *PVALB*+ and *SST*+ cells, generated by scVelo. The color bar above the heatmap denotes cell types and follows the same color scheme shown in **Figure 3A**. C. Immunostaining validation of the *PVALB SST* shared driver gene, calcyon neuron-specific vesicular protein (*CALY*). DAPI, nuclei. Scale bar, 40 μm (left panel) and 20 μm (right four panels). D. Dotplot showing the putative driver gene expression in MGE-derived cells.

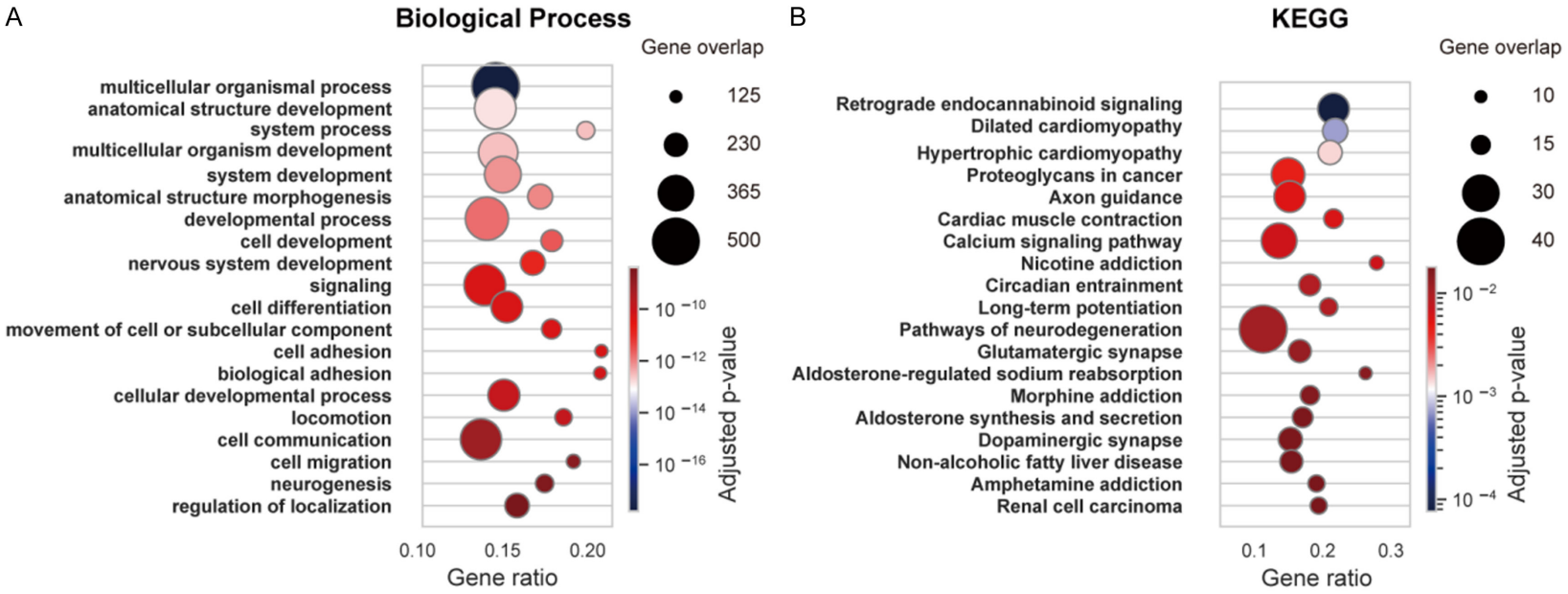

Figure 5. Functional enrichment analysis of latent time-related genes reveals their major roles in nervous system development and axon genesis. A. Dotplot showing the Gene Ontology (GO) biological process enrichment analysis. B. Dotplot showing the Kyoto Encyclopedia of Genes and Genomes (KEGG) pathway enrichment analysis.

tal cataracts can disrupt the development of retinal neural circuits [56, 57]. Similarly, elevated anxiety symptoms are associated with delays in the development of neural circuits, while music therapy has been shown to mitigate anxiety and potentially promote healthy neural development [58, 59]. Once the nervous system reaches full maturity, sensory processing capacity varies significantly among species. Primates, leveraging their prior experience and current state, exhibit greater flexibility in handling complex tasks [60]. Such differences in maturation trajectories indicate that primates have evolved enhanced mechanisms to modify intrinsic neural circuits, necessitating both greater plasticity and robust experience-dependent modulation [60, 61].

Interestingly, our results suggest that, despite sharing similar baseline survival mechanisms, primates and rodents develop dramatically different skill sets for handling everyday challenges. This divergence likely stems from differential gene activity related to neuronal development and plasticity. These genes may be crucial to understanding the molecular and cellular mechanisms behind the advanced information-processing capabilities of primates.

RNA velocity and scVelo analyze RNA lineages by comparing the relative abundances of spliced and unspliced RNAs. These methods were developed to study tissue transcriptomic dynamics at the single-cell level and were originally designed for developing tissues. However, their applicability to mature tissue remains uncertain. Despite this, the highly consistent results observed in our study support the idea that RNA velocity and scVelo are reliable tools for inferring transcriptomic shifts in individual neurons. Further validation is required to determine the extent to which these findings can be generalized across different neuronal populations and conditions.

Disclosure of conflict of interest

None.

Address correspondence to: Ningli Wang, Beijing Tongren Eye Center, Beijing Tongren Hospital, Capital Medical University, 1 Dongjiaomin Alley, Dongcheng District, Beijing 100730, China. Tel: +86-010-58265922; E-mail: wningli@vip.163.com

References

[1] Hao ZZ, Wei JR, Xiao D, Liu R, Xu N, Tang L, Huang M, Shen Y, Xing C, Huang W, Liu X, Xiang M, Liu Y, Miao Z and Liu S. Single-cell transcriptomics of adult macaque hippocampus reveals neural precursor cell populations. Nat Neurosci 2022; 25: 805-817.

[2] Wei JR, Hao ZZ, Xu C, Huang M, Tang L, Xu N, Liu R, Shen Y, Teichmann SA, Miao Z and Liu S. Identification of visual cortex cell types and species differences using single-cell RNA sequencing. Nat Commun 2022; 13: 6902.

[3] Adams DL, Sincich LC and Horton JC. Complete pattern of ocular dominance columns in human primary visual cortex. J Neurosci 2007; 27: 10391-10403.

[4] Zeng H, Shen EH, Hohmann JG, Oh SW, Bernard A, Royall JJ, Glattfelder KJ, Sunkin SM, Morris JA, Guillozet-Bongaarts AL, Smith KA, Ebbert AJ, Swanson B, Kuan L, Page DT, Overly CC, Lein ES, Hawrylycz MJ, Hof PR, Hyde TM, Kleinman JE and Jones AR. Large-scale cellular-resolution gene profiling in human neocortex reveals species-specific molecular signatures. Cell 2012; 149: 483-496.

[5] Bernard A, Lubbers LS, Tanis KQ, Luo R, Podtelezhnikov AA, Finney EM, McWhorter MM, Serikawa K, Lemon T, Morgan R, Copeland C, Smith K, Cullen V, Davis-Turak J, Lee CK, Sunkin SM, Loboda AP, Levine DM, Stone DJ, Hawrylycz MJ, Roberts CJ, Jones AR, Geschwind DH and Lein ES. Transcriptional architecture of the primate neocortex. Neuron 2012; 73: 1083-1099.

[6] Castaldi E, Lunghi C and Morrone MC. Neuroplasticity in adult human visual cortex. Neurosci Biobehav Rev 2020; 112: 542-552.

[7] Shen Y, Shao M, Hao ZZ, Huang M, Xu N and Liu S. Multimodal nature of the single-cell primate brain atlas: morphology, transcriptome, electrophysiology, and connectivity. Neurosci Bull 2024; 40: 517-532.

[8] Xiao W, Qiu WC and Liu HT. From barn lanterns to the 5G intelligent ophthalmic cruiser: the perspective of artificial intelligence and digital technologies on the modality and efficiency of blindness prevention in China. Eye Sci 2024; 1: 1-6.

[9] Berg J, Sorensen SA, Ting JT, Miller JA, Chartrand T, Buchin A, Bakken TE, Budzillo A, Dee N, Ding SL, Gouwens NW, Hodge RD, Kalmbach B, Lee C, Lee BR, Alfiler L, Baker K, Barkan E, Beller A, Berry K, Bertagnolli D, Bickley K, Bomben J, Braun T, Brouner K, Casper T, Chong P, Crichton K, Dalley R, de Frates R, Desta T, Lee SD, D'Orazi F, Dotson N, Egdorf T, Enstrom R, Farrell C, Feng D, Fong O, Furdan S, Galakhova AA, Gamlin C, Gary A, Glandon A,

Goldy J, Gorham M, Goriounova NA, Gratiy S, Graybuck L, Gu H, Hadley K, Hansen N, Heistek TS, Henry AM, Heyer DB, Hill D, Hill C, Hupp M, Jarsky T, Kebede S, Keene L, Kim L, Kim MH, Kroll M, Latimer C, Levi BP, Link KE, Mallory M, Mann R, Marshall D, Maxwell M, McGraw M, McMillen D, Melief E, Mertens EJ, Mezei L, Mihut N, Mok S, Molnar G, Mukora A, Ng L, Ngo K, Nicovich PR, Nyhus J, Olah G, Oldre A, Omstead V, Ozsvar A, Park D, Peng H, Pham T, Pom CA, Potekhina L, Rajanbabu R, Ransford S, Reid D, Rimorin C, Ruiz A, Sandman D, Sulc J, Sunkin SM, Szafer A, Szemenyei V, Thomsen ER, Tieu M, Torkelson A, Trinh J, Tung H, Wakeman W, Waleboer F, Ward K, Wilbers R, Williams G, Yao Z, Yoon JG, Anastassiou C, Arkhipov A, Barzo P, Bernard A, Cobbs C, de Witt Hamer PC, Ellenbogen RG, Esposito L, Ferreira M, Gwinn RP, Hawrylycz MJ, Hof PR, Idema S, Jones AR, Keene CD, Ko AL, Murphy GJ, Ng L, Ojemann JG, Patel AP, Phillips JW, Silbergeld DL, Smith K, Tasic B, Yuste R, Segev I, de Kock CPJ, Mansvelder HD, Tamas G, Zeng H, Koch C and Lein ES. Human neocortical expansion involves glutamatergic neuron diversification. Nature 2021; 598: 151-158.

[10] Zeisel A, Hochgerner H, Lönnerberg P, Johnsson A, Memic F, van der Zwan J, Häring M, Braun E, Borm LE, La Manno G, Codeluppi S, Furlan A, Lee K, Skene N, Harris KD, Hjerling-Leffler J, Arenas E, Ernfors P, Marklund U and Linnarsson S. Molecular architecture of the mouse nervous system. Cell 2018; 174: 999-1014, e1022.

[11] Saunders A, Macosko EZ, Wysoker A, Goldman M, Krienen FM, de Rivera H, Bien E, Baum M, Bortolin L, Wang S, Goeva A, Nemesh J, Kamitaki N, Brumbaugh S, Kulp D and McCarroll SA. Molecular diversity and specializations among the cells of the adult mouse brain. Cell 2018; 174: 1015-1030, e1016.

[12] Tasic B, Menon V, Nguyen TN, Kim TK, Jarsky T, Yao Z, Levi B, Gray LT, Sorensen SA, Dolbeare T, Bertagnolli D, Goldy J, Shapovalova N, Parry S, Lee C, Smith K, Bernard A, Madisen L, Sunkin SM, Hawrylycz M, Koch C and Zeng H. Adult mouse cortical cell taxonomy revealed by single cell transcriptomics. Nat Neurosci 2016; 19: 335-346.

[13] Zeisel A, Muñoz-Manchado AB, Codeluppi S, Lönnerberg P, La Manno G, Juréus A, Marques S, Munguba H, He L, Betsholtz C, Rolny C, Castelo-Branco G, Hjerling-Leffler J and Linnarsson S. Cell types in the mouse cortex and hippocampus revealed by single-cell RNA-seq. Science 2015; 347: 1138-1142.

[14] Zhang Z, Zhou J, Tan P, Pang Y, Rivkin AC, Kirchgessner MA, Williams E, Lee CT, Liu H, Franklin AD, Miyazaki PA, Bartlett A, Aldridge AI, Vu M, Boggeman L, Fitzpatrick C, Nery JR, Castanon RG, Rashid M, Jacobs MW, Ito-Cole T, O'Connor C, Pinto-Duartec A, Dominguez B, Smith JB, Niu SY, Lee KF, Jin X, Mukamel EA, Behrens MM, Ecker JR and Callaway EM. Epigenomic diversity of cortical projection neurons in the mouse brain. Nature 2021; 598: 167-173.

[15] Lake BB, Chen S, Sos BC, Fan J, Kaeser GE, Yung YC, Duong TE, Gao D, Chun J, Kharchenko PV and Zhang K. Integrative single-cell analysis of transcriptional and epigenetic states in the human adult brain. Nat Biotechnol 2018; 36: 70-80.

[16] Tang L, Xu N, Huang M, Yi W, Sang X, Shao M, Li Y, Hao ZZ, Liu R, Shen Y, Yue F, Liu X, Xu C and Liu S. A primate nigrostriatal atlas of neuronal vulnerability and resilience in a model of Parkinson's disease. Nat Commun 2023; 14: 7497.

[17] Bergen V, Lange M, Peidli S, Wolf FA and Theis FJ. Generalizing RNA velocity to transient cell states through dynamical modeling. Nat Biotechnol 2020; 38: 1408-1414.

[18] La Manno G, Soldatov R, Zeisel A, Braun E, Hochgerner H, Petukhov V, Lidschreiber K, Kastriti ME, Lönnerberg P, Furlan A, Fan J, Borm LE, Liu Z, van Bruggen D, Guo J, He X, Barker R, Sundström E, Castelo-Branco G, Cramer P, Adameyko I, Linnarsson S and Kharchenko PV. RNA velocity of single cells. Nature 2018; 560: 494-498.

[19] Wolf FA, Angerer P and Theis FJ. SCANPY: large-scale single-cell gene expression data analysis. Genome Biol 2018; 19: 15.

[20] Wolock SL, Lopez R and Klein AM. Scrublet: computational identification of cell doublets in single-cell transcriptomic data. Cell Syst 2019; 8: 281-291, e289.

[21] Korsunsky I, Millard N, Fan J, Slowikowski K, Zhang F, Wei K, Baglaenko Y, Brenner M, Loh PR and Raychaudhuri S. Fast, sensitive and accurate integration of single-cell data with Harmony. Nat Methods 2019; 16: 1289-1296.

[22] Becht E, McInnes L, Healy J, Dutertre CA, Kwok IWH, Ng LG, Ginhoux F and Newell EW. Dimensionality reduction for visualizing single-cell data using UMAP. Nat Biotechnol 2018; [Epub ahead of print].

[23] Laurens VDM and Hinton G. Visualizing data using t-SNE. J Mach Learn Res 2008; 9: 2579-2605.

[24] Amir el AD, Davis KL, Tadmor MD, Simonds EF, Levine JH, Bendall SC, Shenfeld DK, Krishnaswamy S, Nolan GP and Pe'er D. viSNE enables visualization of high dimensional single-cell data and reveals phenotypic heterogeneity of leukemia. Nat Biotechnol 2013; 31: 545-552.

[25] Pedregosa F, Varoquaux G, Gramfort A, Michel V, Thirion B, Grisel O, Blondel M, Prettenhofer P, Weiss R, Dubourg V, Vanderplas J, Passos A, Cournapeau D, Brucher M, Perrot M and Duchesnay É. Scikit-learn: machine learning in python. J Mach Learn Res 2011; 12: 2825-2830.
[26] Blondel VD, Guillaume JL, Lambiotte R and Lefebvre E. Fast unfolding of communities in large networks. J Stat Mech 2008; 2008: P10008.
[27] Miao Z, Moreno P, Huang N, Papatheodorou I, Brazma A and Teichmann SA. Putative cell type discovery from single-cell gene expression data. Nat Methods 2020; 17: 621-628.
[28] Finak G, McDavid A, Yajima M, Deng J, Gersuk V, Shalek AK, Slichter CK, Miller HW, McElrath MJ, Prlic M, Linsley PS and Gottardo R. MAST: a flexible statistical framework for assessing transcriptional changes and characterizing heterogeneity in single-cell RNA sequencing data. Genome Biol 2015; 16: 278.
[29] Ashburner M, Ball CA, Blake JA, Botstein D, Butler H, Cherry JM, Davis AP, Dolinski K, Dwight SS, Eppig JT, Harris MA, Hill DP, Issel-Tarver L, Kasarskis A, Lewis S, Matese JC, Richardson JE, Ringwald M, Rubin GM and Sherlock G. Gene ontology: tool for the unification of biology. The gene ontology consortium. Nat Genet 2000; 25: 25-29.
[30] Consortium GO. The gene ontology resource: enriching a gold mine. Nucleic Acids Res 2021; 49: D325-D334.
[31] Kanehisa M and Goto S. Kegg: Kyoto encyclopedia of genes and genomes. Nucleic Acids Res 2000; 28: 27-30.
[32] Kanehisa M. Toward understanding the origin and evolution of cellular organisms. Protein Sci 2019; 28: 1947-1951.
[33] Kanehisa M, Furumichi M, Sato Y, Ishiguro-Watanabe M and Tanabe M. KEGG: integrating viruses and cellular organisms. Nucleic Acids Res 2021; 49: D545-D551.
[34] Mootha VK, Lindgren CM, Eriksson KF, Subramanian A, Sihag S, Lehar J, Puigserver P, Carlsson E, Ridderstråle M, Laurila E, Houstis N, Daly MJ, Patterson N, Mesirov JP, Golub TR, Tamayo P, Spiegelman B, Lander ES, Hirschhorn JN, Altshuler D and Groop LC. PGC-1alpha-responsive genes involved in oxidative phosphorylation are coordinately downregulated in human diabetes. Nat Genet 2003; 34: 267-273.
[35] Subramanian A, Tamayo P, Mootha VK, Mukherjee S, Ebert BL, Gillette MA, Paulovich A, Pomeroy SL, Golub TR, Lander ES and Mesirov JP. Gene set enrichment analysis: a knowledge-based approach for interpreting genome-wide expression profiles. Proc Natl Acad Sci U S A 2005; 102: 15545-15550.
[36] Raudvere U, Kolberg L, Kuzmin I, Arak T, Adler P, Peterson H and Vilo J. g:Profiler: a web server for functional enrichment analysis and conversions of gene lists (2019 update). Nucleic Acids Res 2019; 47: W191-W198.
[37] Haeussler M, Zweig AS, Tyner C, Speir ML, Rosenbloom KR, Raney BJ, Lee CM, Lee BT, Hinrichs AS, Gonzalez JN, Gibson D, Diekhans M, Clawson H, Casper J, Barber GP, Haussler D, Kuhn RM and Kent WJ. The UCSC genome browser database: 2019 update. Nucleic Acids Res 2019; 47: D853-D858.
[38] Lim L, Mi D, Llorca A and Marín O. Development and functional diversification of cortical interneurons. Neuron 2018; 100: 294-313.
[39] Inan M, Welagen J and Anderson SA. Spatial and temporal bias in the mitotic origins of somatostatin- and parvalbumin-expressing interneuron subgroups and the chandelier subtype in the medial ganglionic eminence. Cereb Cortex 2012; 22: 820-827.
[40] Miyoshi G, Butt SJB, Takebayashi H and Fishell G. Physiologically distinct temporal cohorts of cortical interneurons arise from telencephalic Olig2-expressing precursors. J Neurosci 2007; 27: 7786-7798.
[41] Feng W, Li Y, Dao P, Aburas J, Islam P, Elbaz B, Kolarzyk A, Brown AE and Kratsios P. A terminal selector prevents a Hox transcriptional switch to safeguard motor neuron identity throughout life. Elife 2020; 9: e50065.
[42] Blasco H, Bernard-Marissal N, Vourc'h P, Guettard YO, Sunyach C, Augereau O, Khederchah J, Mouzat K, Antar C, Gordon PH, Veyrat-Durebex C, Besson G, Andersen PM, Salachas F, Meininger V, Camu W, Pettmann B, Andres CR and Corcia P. A rare motor neuron deleterious missense mutation in the DPYSL3 (CRMP4) gene is associated with ALS. Hum Mutat 2013; 34: 953-960.
[43] Ataman B, Boulting GL, Harmin DA, Yang MG, Baker-Salisbury M, Yap EL, Malik AN, Mei K, Rubin AA, Spiegel I, Durresi E, Sharma N, Hu LS, Pletikos M, Griffith EC, Partlow JN, Stevens CR, Adli M, Chahrour M, Sestan N, Walsh CA, Berezovskii VK, Livingstone MS and Greenberg ME. Evolution of osteocrin as an activity-regulated factor in the primate brain. Nature 2016; 539: 242-247.
[44] Müller T, Reichlmeir M, Hau AC, Wittig I and Schulte D. The neuronal transcription factor MEIS2 is a calpain-2 protease target. J Cell Sci 2024; 137: jcs261482.
[45] Nitarska J, Smith JG, Sherlock WT, Hillege MMG, Nott A, Barshop WD, Vashisht AA, Wohlschlegel JA, Mitter R and Riccio A. A functional switch of NuRD chromatin remodeling complex subunits regulates mouse cortical development. Cell Rep 2016; 17: 1683-1698.

[46] Muthusamy N, Chen YJ, Yin DM, Mei L and Bergson C. Complementary roles of the neuron-enriched endosomal proteins NEEP21 and calcyon in neuronal vesicle trafficking. J Neurochem 2015; 132: 20-31.
[47] Gottschall PE and Howell MD. ADAMTS expression and function in central nervous system injury and disorders. Matrix Biol 2015; 44-46: 70-76.
[48] Pederick DT, Homan CC, Jaehne EJ, Piltz SG, Haines BP, Baune BT, Jolly LA, Hughes JN, Gecz J and Thomas PQ. Pcdh19 loss-of-function increases neuronal migration in vitro but is dispensable for brain development in mice. Sci Rep 2016; 6: 26765.
[49] Moncayo JA, Ayala IN, Argudo JM, Aguirre AS, Parwani J, Pachano A, Ojeda D, Cordova S, Mora MG, Tapia CM and Ortiz JF. Understanding protein protocadherin-19 (PCDH19) syndrome: a literature review of the pathophysiology. Cureus 2022; 14: e25808.
[50] Lončarić M, Stojanović N, Rac-Justament A, Coopmans K, Majhen D, Humphries JD, Humphries MJ and Ambriović-Ristov A. Talin2 and KANK2 functionally interact to regulate microtubule dynamics, paclitaxel sensitivity and cell migration in the MDA-MB-435S melanoma cell line. Cell Mol Biol Lett 2023; 28: 56.
[51] Kolb H, Fernandez E, Nelson R, editors. Webvision: the organization of the retina and visual system. Salt Lake City (UT): University of Utah Health Sciences Center, 1995.
[52] Balaram P and Kaas JH. Towards a unified scheme of cortical lamination for primary visual cortex across primates: insights from NeuN and VGLUT2 immunoreactivity. Front Neuroanat 2014; 8: 81.
[53] Dumoulin SO and Wandell BA. Population receptive field estimates in human visual cortex. NeuroImage 2008; 39: 647-660.
[54] Martinez P and Sprecher SG. Of circuits and brains: the origin and diversification of neural architectures. Front Ecol Evol 2020; 8: 82.
[55] Danka Mohammed CP and Khalil R. Postnatal development of visual cortical function in the mammalian brain. Front Syst Neurosci 2020; 14: 29.
[56] Zou YS, Li YQ and Liu ZZ. The statusquo and advances in categorization of congenital cataract. Eye Sci 2024; 1: 56-66.
[57] Zhang F and Zhao YE. Research on retinal mechanism of deprivation amblyopia due to congenital cataracts. Int Rev Ophthalmol 2018; 42: 414.
[58] Liu Z, Hu Y, Zhang Y, Liu W, Zhang L, Wang Y, Yang H, Wu J, Cheng W and Yang Z. Altered gray matter volume and structural co-variance in adolescents with social anxiety disorder: evidence for a delayed and unsynchronized development of the fronto-limbic system. Psychol Med 2021; 51: 1742-1751.
[59] Fu Q, Li S, Wang F and Tian B. Effects of music therapy on the anxiety level and physiological responses of patients undergoing ophthalmic surgery: a systematic review and meta-analysis. 2024.
[60] Roberts AC and Clarke HF. Why we need nonhuman primates to study the role of ventromedial prefrontal cortex in the regulation of threat- and reward-elicited responses. Proc Natl Acad Sci U S A 2019; 116: 26297-26304.
[61] Sousa AMM, Meyer KA, Santpere G, Gulden FO and Sestan N. Evolution of the human nervous system function, structure, and development. Cell 2017; 170: 226-247.